ACS APPLIED MATERIALS & INTERFACES

Research Article

www.acsami.org

High Current Density and Longtime Stable Field Electron Transfer from Large-Area Densely Arrayed Graphene Nanosheet–Carbon Nanotube Hybrids

Jian-Hua Deng,*[,†] Lin Cheng,[†] Fan-Jie Wang,[†] Guo-Zheng Li,[†] De-Jun Li,[†] and Guo-An Cheng*[,‡]

[†]College of Physics and Materials Science, Tianjin Normal University, Tianjin 300387, People's Republic of China

[‡]Key Laboratory of Beam Technology and Material Modification of Ministry of Education, Beijing Normal University, Beijing 100875, People's Republic of China

Supporting Information

ABSTRACT: Achieving high current and longtime stable field emission from large area (larger than 1 mm^2), densely arrayed emitters is of great importance in applications for vacuum electron sources. We report here the preparation of graphene nanosheet–carbon nanotube (GNS–CNT) hybrids by following a process of iron ion prebombardment on Si wafers, catalyst-free growth of GNSs on CNTs, and high-temperature annealing. Structural observations indicate that the iron ion prebombardment influences the growth of CNTs quite limitedly, and the self-assembled GNSs sparsely distributed on the tips of CNTs with their sharp edges unfolded outside. The field emission study indicates that the maximum emission current density (J_{max}) is gradually promoted after these treatments, and the composition with GNSs is helpful for decreasing the operation fields of CNTs. An optimal J_{max} up to 85.10 mA/cm^2 is achieved from a 4.65 mm^2 GNS–CNT sample, far larger than 7.41 mA/cm^2 for the as-grown CNTs. This great increase of J_{max} is ascribed to the reinforced adhesion of GNS–CNT hybrids to substrates. We propose a rough calculation and find that this adhesion is promoted by 7.37 times after the three-step processing. We consider that both the ion prebombardment produced rough surface and the wrapping of CNT foot by catalyst residuals during thermal processing are responsible for this enhanced adhesion. Furthermore, the three-step prepared GNS–CNT hybrids present excellent field emission stability at high emission current densities (larger than 20 mA/cm^2) after being perfectly aged.

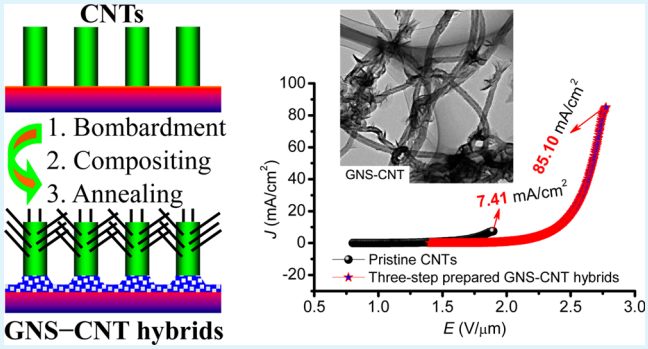

KEYWORDS: *carbon nanotube, graphene nanosheet, hybrids, adhesion, field emission*

1. INTRODUCTION

High-performance field emission (FE) often requires emitters to have low turn-on electric field (E_{on}, applied field at 10 $\mu A/cm^2$) and threshold field (E_{th}, applied field at 10 mA/cm^2) and, importantly, excellent FE stability at large emission currents. Carbon nanotubes (CNTs) and graphenes are two promising FE materials due to their unique characteristics such as diverse electrical properties, chemical inertness, and outstanding mechanical strength.[1−7] They have aroused a great many FE applications such as flat panel displays,[8,9] liquid crystal displays,[10] X-ray sources,[11] lighting lamps,[12] and so on. CNTs have large aspect ratios of large lengths (μm) and small diameters (nm), which greatly facilitates electron tunneling through barriers and thus makes them good candidates in applications requiring low E_{on} and E_{th}.[5,13] However, the small diameters of CNTs also make them more likely to be burned out during FE because of the gradually accumulated Joule heat especially for field electron transfer at high currents,[14,15] while for graphene, its unique two-dimensional structure is advantageous for large current transferring and faster heat dispersion, which greatly weakens the Joule heating induced burning of active emission sites and thus improves its FE stability.[2,6] It is thus promising to fabricate hybrids having both the FE advantages of CNTs and graphenes. Field electron transfer from hybrid nanomaterials has been well reported in recent years.[16−19] For example, Liu et al. reported the FE performance of a hybrid nanomaterial composed of ZnO nanoparticles and CuTCNQ (copper 7,7,8,8-tetracyanoquinodimethane) nanowires, and they found that the maximum emission current density (J_{max}) of the hybrid ZnO–CuTCNQ nanowires was six times that of the CuTCNQ nanowire array.[16] The composition between graphene and CNTs has also been well reported in recent years. For example, Zanin et al. reported the fabrication of reduced graphene oxide and vertically aligned CNTs superhydrophilic films as high-performance supercapacitors.[20] Liu et al. employed a one-step approach to fabricating graphene

Received: September 24, 2014
Accepted: October 22, 2014
Published: October 22, 2014

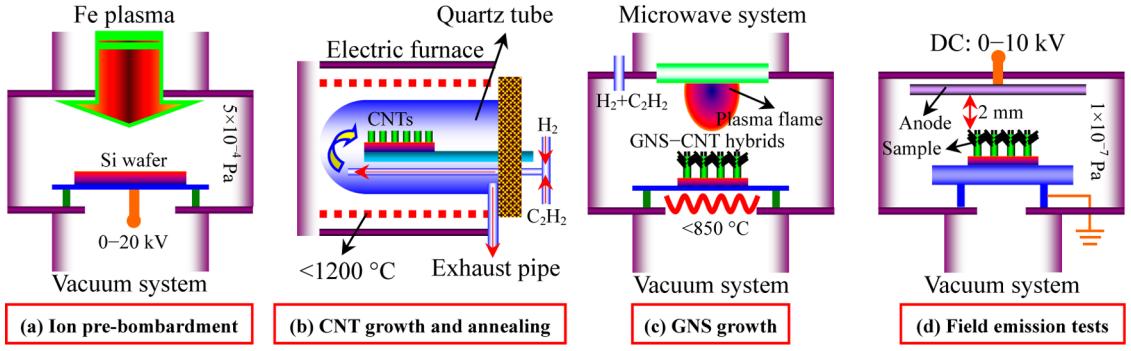

Figure 1. Schematics of the setups used for sample preparations. (a) The metal vapor vacuum arc ion source used for the iron ion prebombardment on Si wafers. (b) The tubular furnace used for the growth of CNTs and the high-temperature annealing of our samples. (c) The microwave PECVD system used for the growth of GNSs on CNTs. (d) The classical diode setup used for the FE tests.

sheet–carbon nanotube (GS–CNT) composites and studied their FE properties.[21] The GS–CNT composites they prepared have a low E_{on} of ~0.6 V/μm and a good FE stability with only 8% current decline after 10 h of continuous emission. We have also reported the self-assembled growth of graphenes on chemical vapor deposition (CVD) prepared CNTs by using radio frequency sputtering.[22] In comparison with as-grown CNTs, the graphene–CNT hybrids have lower E_{on} and E_{th} and better FE stability, in good agreement with our anticipation. However, the J_{max} of these hybrids is usually smaller than 20 mA/cm^2, which is detrimental in practical applications requiring large current and longtime stable field electron transfer, such as X-ray tubes and lighting lamps. The J_{max} is obtained when part of the emitters is extracted from substrates and a current breakdown occurs concomitantly. This current breakdown is irreversible and is quite different from the restorable current fluctuations or spikes during FE tests.[23] In this regard, improving the adhesion between emitters and substrates is an effective approach to promoting the J_{max}. Previous studies show that predepositing a Ni buffer layer on substrates can enhance the adhesion due to the high adhesive strength of Ni,[24,25] but for CVD prepared CNTs, this method is not feasible because the Ni is also a catalyst for the growth of CNTs; that is, the wetting Ni layer will influence the growth of CNTs simultaneously. It is thus important to develop a new strategy to improve the adhesion of CVD CNTs to substrates. Previous studies of FE from CNTs have reported J_{max} from several mA/cm^2 to as large as 4 A/cm^2.[2,23,26–32] However, these CNT emitters are often associated with small areas. For example, Thong et al. obtained a J_{max} of 0.5 A/cm^2 from a 3.6 × 10^{-3} cm^2 CNT array;[23] Sohn et al. reported a J_{max} of 80 mA/cm^2 at an area of 4 × 10^{-5} cm^2 from multiwalled CNTs,[29] and even an outstanding J_{max} up to 100 A/cm^2 can be deduced if localized emission is assumed.[32] It should be mentioned that the practical J_{max} is known to fall off sharply with the increase of cathode areas.[33] Therefore, achieving high current FE from large area emitters is difficult but of great importance in applications. However, to the best of our knowledge, there has been few reports of FE with a J_{max} more than 50 mA/cm^2 from densely arrayed CNT-based emitters with areas on the order of magnitude of 10^{-2} cm^2.

In the present study, graphene nanosheet–carbon nanotube (GNS–CNT) hybrids were prepared on iron ion bombarded Si wafers by using microwave plasma enhanced chemical vapor deposition (PECVD) and then annealed at high temperatures. The processed GNS–CNT hybrids are found to have a far larger J_{max} than that of the pristine CVD CNTs and also have excellent FE stability at high emission currents.

2. EXPERIMENTAL SECTION

2.1. Iron Ion Prebombardment on Si Wafers. Two types of substrates, pristine and iron ion bombarded Si wafers, were used to grow CNTs for comparison, and we name them here as Si and Fe–Si substrates for convenience, respectively. For all Si wafers, they were first immersed into a diluted hydrofluoric acid (Vol. 4%) solution to remove the SiO_2 termination on their surfaces. The Fe–Si substrates were prepared in vacuum (5 × 10^{-4} Pa) by using a metal vapor vacuum arc (MEVVA) ion source system at room temperature, as schematically shown in Figure 1a. The iron plasma was generated by using arc discharge on a high-purity iron rod. A negative bias of ~10 kV was applied on the Si wafers to perform the ion bombardment. The processing time was 15 min.

2.2. Preparation of CNTs. The CNT growth was carried out in a tubular furnace at ambient pressure by using the traditional thermal CVD.[22] Figure 1b schematically shows this furnace. It is composed of an electric furnace and a quartz tube. For both Si and Fe–Si wafers, a 5 nm-thick iron film was first deposited on their surfaces by using magnetron sputtering to act as a catalyst. The catalyst was first processed at 580 °C for 1 h under 400 sccm H_2 and then etched at 750 °C for 10 min under 150 sccm NH_3 to promote the its activity. The CNT growth was taken under 600 sccm H_2 and 87 sccm C_2H_2 at 750 °C. The growth time was 30 min.

2.3. Preparation of GNS–CNT Hybrids. The growth of GNSs on the thus prepared CNTs was performed by using microwave (2.45 GHz) PECVD. Figure 1c shows a schematic of this setup. C_2H_2 and H_2 were used as the carbon feedback and the assisted gas, respectively. Different from the catalyzed growth of CNTs, the GNS growth is catalyst-free. The substrate temperature was controlled by using an originally designed graphitic heater. The GNS growth was taken under 800 °C, 1 kPa, 150 W, 1 sccm C_2H_2, and 10 sccm H_2. The growth time was 2 h. The distance between the plasma flame and our samples was ~1 cm.

2.4. High-Temperature Annealing. The GNS–CNT hybrids were annealed at elevated temperatures to study the influence of temperature processing on their FE performance. This was carried out in the same tubular furnace that was used in the preparation of CNTs, as shown in Figure 1b. H_2 was used as the protecting gas.

2.5. Structural Characterizations. The structures of our samples were characterized by using a scanning electron microscope (SEM, S–4800, Hitachi, Japan, 10 kV). Transmission electron microscopy (TEM, JEM–2010, JEOL, Japan, 200 kV) was employed to observe their fine structure. Raman spectroscopy (LabRAM Aramis, Horiba Jobin Yvon, France) with a He–Ne laser (wavelength: 633 nm) was used to perform the defect analysis and qualitatively evaluate the thickness of GNSs. X-ray photoelectron spectroscopy (XPS, PHI Quantera SXM) using Al Kα irradiation (~1486.6 eV) was used to obtain the chemical bonding information on our samples. The work

dx.doi.org/10.1021/am5065624 | ACS Appl. Mater. Interfaces 2014, 6, 21558–21566

function of our emitters was obtained by using a Photoelectron spectrometer (AC−2, Riken Keiki, Japan, spot area: 4 × 4 mm^2) in atmosphere.

2.6. FE Tests. The FE tests were performed in a vacuum chamber (~1.0×10^{-7} Pa) at room temperature by using a parallel diode setup, as schematically shown in Figure 1d. The prepared samples were used as the cathode against a stainless steel as the anode, and the distance between them was 2 mm. The surfaces of our samples and the anode were kept perfectly parallel to avoid an inhomogeneous electric field. The areas of samples used in the FE tests are larger than 0.04 cm^2. During FE tests, DC voltages ranging from 0 to 10 kV were applied to the anode with a constant increasing rate of 500 V/min while grounding the cathode. The FE results were automatically recorded by a computer in terms of emission current (I) versus applied voltage (V).

3. RESULTS AND DISCUSSION

3.1. Morphology of CNTs Prepared on Si and Fe−Si Wafers. We anticipate that the bombarded iron layer will reinforce the adhesion of CNTs to substrates but will not influence the growth of CNTs. In this regard, we examined the catalytic effectiveness of the bombarded iron film. Fe−Si wafers without the magnetron sputtering deposited 5 nm iron film was used as the substrates for CNT growth, as shown in Figure 2a.

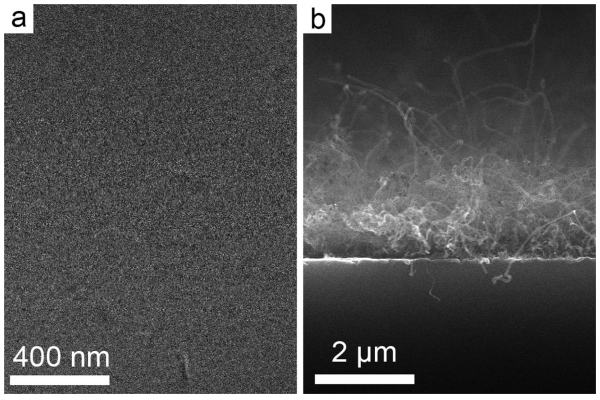

Figure 2. SEM images for CNTs grown on (a) high-energy iron ion bombarded Si wafers and (b) low-energy deposited 10 nm iron film terminated Si wafers.

It can be seen that, after the regular CNT growth steps, no CNT grows on the wafers, indicating that the bombarded iron films have no catalytic action. We consider that the implanted iron ions exist in the forms of interstitials in the Si lattice and it is hard to be precipitated at the CNT growth temperature (750 °C). It is tempting to think that if we replace the iron ion bombardment by low-energy deposition we can still obtain the CNTs that we expected. To figure this out, a low negative bias of 100 V was applied on our samples during the preparation of Fe−Si wafers by using the MEVVA source, and the processing time was also 15 min, after which an iron film of ~10 nm was deposited. These Fe−Si wafers were then used to grow CNTs in regular steps, which certainly include the following deposition of the 5 nm iron catalyst film by using magnetron sputtering. Figure 2b shows the SEM image of thus prepared CNTs. They are sparsely distributed and badly aligned on Si wafers. We attribute this to the fact that the MEVVA deposited 10 nm iron film can also act as a catalyst for the CNT growth, resulting in the increase of catalyst thickness, and thus influences the ultimate morphology of CNTs. These badly aligned CNTs are not suitable for FE for lack of enough active emission sites.

Figure 3a,b shows the side-view SEM images of CNTs grown on Si and Fe−Si wafers, respectively. In comparison with the

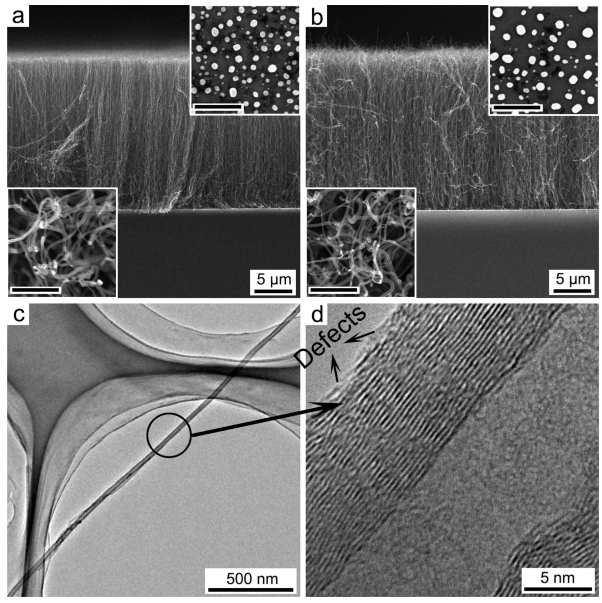

Figure 3. Side-view SEM images of CNTs grown on (a) Si and (b) Fe−Si wafers, and the bottom-left insets are the corresponding top-view SEM images. The top-right insets are the corresponding top-view SEM images of the catalyst before the growth of CNTs. (c) Low- and (d) high-resolution TEM images of a single CNT. Scale bars in the insets of (a) and (b) are 500 nm.

sparsely distributed CNTs shown in Figure 2b, these CNTs are densely arrayed and both of them are ~20 μm in length. However, the CNTs grown on the Si wafers are aligned in a more orderly fashion and thus slightly denser than those prepared on the Fe−Si wafers. The density difference of these two types of CNTs can be clearly seen from the amplified side-view SEM images shown in Figure S1 of the Supporting Information (Page S1). We figured this out by observing the morphology of the catalyst before the growth of CNTs, as shown in the top-right insets of Figure 3a,b. It can be seen that the aggregated catalyst clusters on the Si wafers are denser than those on the Fe−Si ones, which directly results in the relatively higher density of CNTs on the Si wafers. However, we still do not know the exact cause for this different catalyst distribution, which needs to be further studied in the future. The bottom-left insets of Figure 3a,b are the corresponding top-view SEM images of these two types of CNTs. They are both 20−30 nm in diameter and have well-separated tips. The above SEM observations indicate that the ion prebombardment puts a quite limited influence on the growth of CNTs, in good agreement with our anticipation. Given this, we only chose one type of CNTs for the following TEM observation. Figure 3c shows a low-resolution TEM image of a single CNT. This CNT has the typical tubular structure. Its fine structure is shown in Figure 3d. It has the typical layered structure and also has defects at its tube walls. For FE consideration, these defects are believed to enhance electron transfer by means of introducing new active emission sites.[34]

3.2. FE Properties of CNTs Grown on Si and Fe−Si Wafers. The FE performance of the above-mentioned two types of CNTs was tested for comparison. A circular testing model was employed. In this model, voltages are circularly

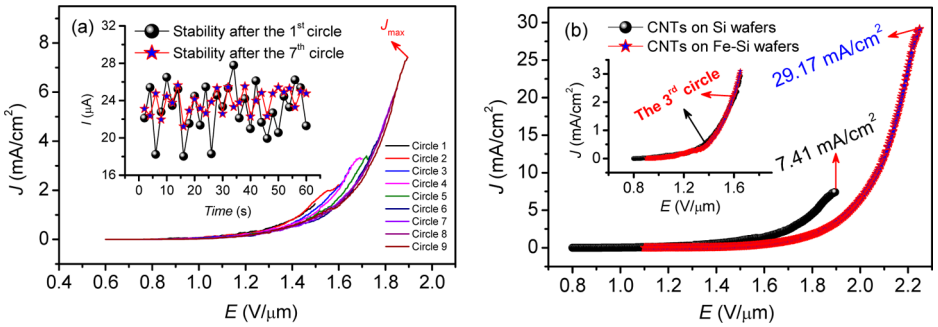

Figure 4. (a) FE J–E curves of different testing circles for CNTs grown on Si wafers. The inset plots their 60 s FE stability at ~20 μA, presented in terms of I versus time. These curves are obtained right after the 1st and the 7th J–E testing circles. (b) FE J–E curves of the last testing circles for CNTs grown on Si and Fe–Si wafers showing their J_{max}, and the inset is the FE J–E curves of the 3rd testing circle for these two types of CNTs.

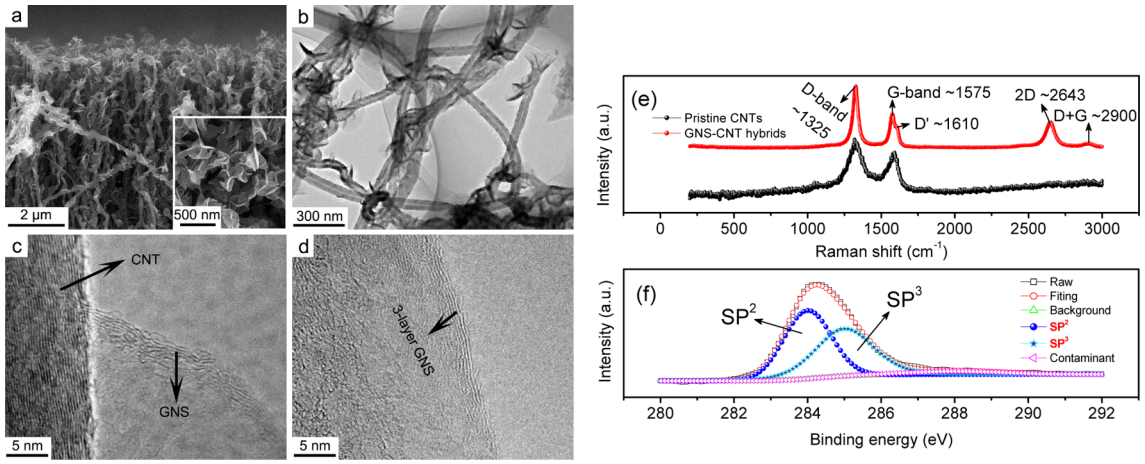

Figure 5. (a) Side-view SEM image of GNS–CNT hybrids and (inset) the corresponding top-view SEM image. (b) Low-resolution TEM image of GNS–CNT hybrids showing the sparse distribution of GNSs on CNTs. (c) High-resolution TEM image of a GNS–CNT hybrid. (d) High-resolution TEM image of the edge of a 3-layer GNS. (e) Raman spectra of the pristine CNTs and the GNS–CNT hybrids. (f) XPS spectrum of the C 1s peak for the GNS–CNT hybrids. Deconvolution of this peak shows three component peaks centered at 284, 285, and 288 eV.

applied to the anode with a constant increasing rate of 500 V/min, and we manually increase the upper limit of the voltage span by 50–100 V at the beginning of a new testing circle until the J_{max} is obtained. Figure 4a shows the FE performance in different testing circles for CNTs fabricated on Si wafers (sample area: 4.89×10^{-2} cm^2), presented in terms of emission current density (J) versus applied field (E), i.e., the J–E curves. The FE performance of our emitters is found to degrade gradually with the increase of testing circles. The E_{on} for the first testing circle is only 0.80 V/μm, while that for the last testing circle has increased to 0.97 V/μm. This FE deterioration is ascribed to the aging of CNTs, which arises from the following two causes: (1) the desorption of absorbates on the surface of CNTs due to the attraction of electrostatic force,[35] especially absorbates that are detrimental to FE, such as oxygen[36] and (2) the burning out of loosely bonded and defected CNTs on the top surface of CNT arrays due to the Joule heating effect.[14,15] However, the aging of CNTs is helpful for improving their FE stability. The inset of Figure 4a shows the FE stability of CNTs obtained right after the first and the seventh testing circles, presented in terms of I versus time. The current fluctuation for the seven-circle aged CNTs is far smaller than that for the one-circle aged one, indicating that the FE stability of CNTs improves greatly after the circular tests. Apparently, the J_{max} of CNTs is obtained at the end of the last circle, which corresponds with an irreversible current breakdown. Figure 4b shows the FE J–E curves of the last testing circles for CNTs grown on Si and Fe–Si wafers. The J_{max} for the Fe–Si CNTs is far larger than that for the other ones (29.17 versus 7.41 mA/cm^2), indicating that the J_{max} of CNTs increases dramatically after the iron ion prebombardment on Si wafers. The E_{on} and E_{th} for these two types of CNTs are quite different (Figure 4b). We attribute this to the fact that the total testing circles for the pristine and Fe–Si CNTs are 9 and 17, respectively, and these extra 8 circles make the Fe–Si samples aged more drastically, resulting in their worse FE behavior. In fact, comparison of FE J–E curves of the first several testing circles does not show much difference, no matter what the substrate is, mainly because the CNTs prepared on these two types of substrates have similar morphology (see Figure 3a,b). The inset of Figure 4b shows the FE J–E curves of the third testing circle for CNTs grown on Si and Fe–Si wafers, which are nearly the same.

3.3. Morphology and FE Performance of GNS–CNT Hybrids. To further increase the J_{max} of our emitters, CNTs grown on Fe–Si wafers are used to fabricate GNS–CNT hybrids. Figure 5a shows the SEM image of the GNS–CNT hybrids. It can be seen that the GNSs are sparsely distributed on the CNTs and have sizes of 200–400 nm in diameters, and the GNSs mainly grow at the upper section of the CNTs. This is ascribed to the high density of CNTs that hinders the diffusion of the carbon source into the deep CNT forest. The

dx.doi.org/10.1021/am5065624 | ACS Appl. Mater. Interfaces 2014, 6, 21558–21566

GNSs on the CNTs are well separated with their sharp edges unfolded outside, as shown in the inset of Figure 5a. This morphology is believed to be helpful for FE by facilitating the electron tunneling through barriers, and additionally,[6] the sparse distribution of GNSs can lower the influence of field-screening.[37] Figure 5b is a low-resolution TEM image showing dispersed GNS−CNT hybrids. The CNTs still have their tubular structure, and the GNS−CNT hybrids form a rose-like appearance. Figure 5c is a high-resolution TEM image showing the fine structure of a GNS−CNT hybrid. The CNT has the typical layered structure with defected outer shells, while the layer arrangement for the GNS is irregular. Figure 5d is a high-resolution TEM image of the edge of a 3-layer GNS, indicating the thin nature of our GNSs. Apparently, these sharp edges of GNSs can serve as high-performance emission sites during FE. Further structural information was obtained from the Raman spectroscopy. Figure 5e shows the Raman spectra of pristine CNTs and the GNS−CNT hybrids. For the pristine CNTs, the two most intense features are the D-band at ∼1325 cm^{-1} and the G-band at ∼1575 cm^{-1}. The G peak arises from the doubly degenerate zone center E_{2g} mode, and it is always observed in graphite samples, while the D peak corresponds with the disordered carbon in graphite.[38] The intensity ratio of the disordered carbon related D peak and the graphite carbon related G peak, i.e., I_D/I_G, can be used to qualitatively determine the defects of carbon materials.[39,40] The I_D/I_G ratios for the pristine and the GNS−CNT hybrids are 1.82 and 1.87, respectively, indicating that they both are abundant in defects, in good agreement with the above TEM observations (Figures 3d and 5c,d). These defects are helpful for improving the FE performance of emitters by means of lowering the work function and increasing the electron transferring traces.[34,41] The comparison of the Raman spectrum of the GNS−CNT hybrids with that of the pristine CNTs shows more of a difference. First, a so-called D' peak (at ∼1610 cm^{-1}) is observed at the shoulder of the G peak for the GNS−CNT sample. This peak is ascribed to the presence of microcrystalline in our samples.[39] Second, a prominent peak centered at ∼2643 cm^{-1}, called 2D band, is observed in the GNS−CNT hybrids. The 2D band arises from the second order of zone-boundary phonons, and its position and shape are related to the structure of graphene. The intensity ratio of the 2D peak and the G peak (I_{2D}/I_G) can be used to roughly evaluate the thickness of graphenes. For example, the 2D peak of a single-layer graphene is 4 times more intense than the G peak.[39] Few-layer (less than 10 layers) graphenes are often associated with I_{2D}/I_G ratios approximate or larger than 1.0. The I_{2D}/I_G ratio of the GNS−CNT hybrids is 1.20, suggesting that our GNSs are ultrathin graphenes. The unconspicuous peak centered at ∼2900 cm^{-1} comes from the combination of the D peak and G peak.[39] In addition, the chemical bonding of the carbon atoms in the GNS−CNT hybrids was determined by using XPS. Figure 5f shows the XPS spectrum of the C 1s peak for the GNS−CNT hybrids. Deconvolution of the C 1s peak shows three component peaks centered at 284, 285, and 288 eV, which correspond with sp^2- and sp^3-hybridized carbon[42,43] and the oxygen contamination,[44] respectively. It can be seen that the GNS−CNT hybrids are abundant in sp^3-hybridized defects. A previous study indicates that these distorted sp^3-hybridized defects, quite different from the planar sp^2-hybridized carbon, can improve the FE performance of field emitters by means of introducing new active emission sites.[6,41]

Figure 6 shows the FE $J-E$ curve of GNS−CNT hybrids synthesized on the Fe−Si wafers (sample area: 5.14 × 10^{-2} cm^2). It can be seen that the J_{max} of this sample is 35.27 mA/cm^2, slightly larger than 29.17 mA/cm^2 for CNTs prepared on the Fe−Si wafers, not to mention 7.41 mA/cm^2 for CNTs grown on the Si wafers (Figure 4b). Furthermore, the E_{th} of the GNS−CNT hybrids is 1.88 V/μm, smaller than 2.07 V/μm for CNTs fabricated on the Fe−Si wafers. This increased J_{max} and lower E_{th} from our hybrid emitters are very important in applications. The inset of Figure 6 shows the corresponding Fowler−Nordheim ($F-N$) plots, presented in terms of $\ln(J/E^2)$ versus $1/E$, whose linear relationship indicates typical $F-N$ type FE behavior.[45] The work function of the GNS−CNT hybrids is 4.71 eV, which is obtained by using a photoelectron spectrometer. With the work function and the constant slope in the low-E region of the $F-N$ plots, the field enhancement factor (β) can be determined by using the $F-N$ theory: ∼4516. Apparently, this calculated β is considerably larger than the geometrical β (∼1000) calculated from (h/r) using the height (h, ∼20 μm) and radius (r, ∼20 nm) of the individual emitters, not to mention the influence of field-screening effect,[37] which will greatly decrease the effective geometrical β when the emitters are densely arrayed. This difference in the β is ascribed to the fact that the emission is a multistage process from many adjacent emitting tips rather than being from one isolated tip.[46,47] The defects in our GNS−CNT hybrids can play a role as these active emission tips. This large field enhancement factor (∼4516) of the GNS−CNT hybrids can be ascribed to the following three aspects. Intrinsically, the GNSs have atomic thin edges and their sparse distribution will help them yield extremely large local applied fields at emission sites. Furthermore, the defects at GNS edges form distorted sp^3-hybridized geometry (Figure 5f), which directly leads to the increase of active emission sites.[41] Third, in comparison with planar substrates, the large-aspect-ratio CNTs can also increase the local applied fields at the emission sites of GNSs.

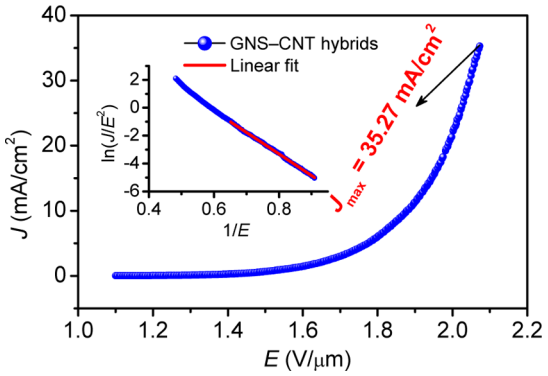

Figure 6. FE $J-E$ curve of GNS−CNT hybrids synthesized on Fe−Si wafers, and the inset is the corresponding $F-N$ plots presented in terms of $\ln(J/E^2)$ versus $1/E$.

3.4. FE Performance of Annealed GNS−CNT Hybrids.

GNS−CNT hybrids prepared on the Fe−Si wafers were annealed at different temperatures to further promote the J_{max}. Figure 7a shows the FE $J-E$ curves of GNS−CNT hybrids after being annealed at 750, 900, and 1050 °C for 2 h and 1050 °C for 5 h. In comparison with the J_{max} of the pristine GNS−CNT hybrids, the J_{max} values for the annealed samples increase dramatically. A large J_{max} up to 85.10 mA/cm^2 is achieved from a 4.65 × 10^{-2} cm^2 GNS−CNT sample after being annealed at

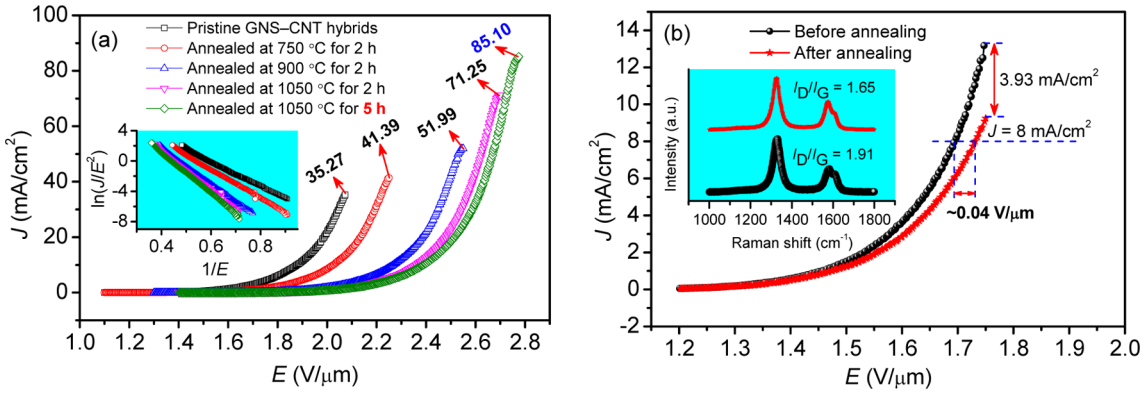

Figure 7. (a) FE J–E curves of GNS–CNT hybrids annealed at different temperatures showing their J_{max}. The inset is the corresponding F–N plots. (b) FE J–E curves of GNS–CNT hybrids before and after being annealed at 1050 °C for 2 h.

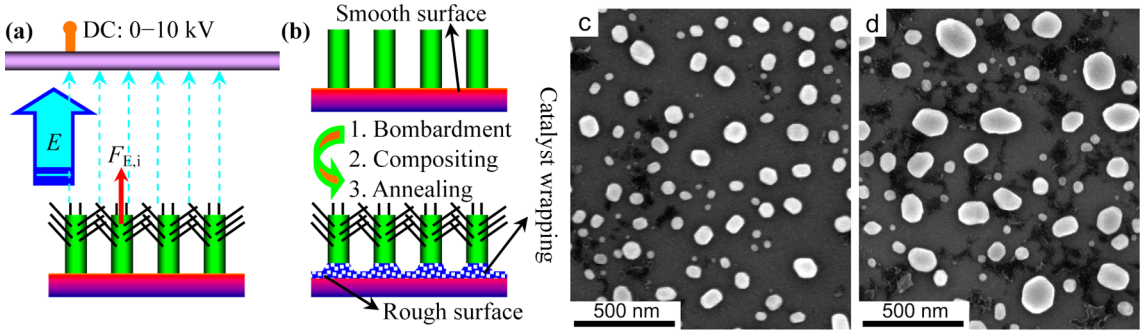

Figure 8. (a) Schematic illustration for the field electron transfer during FE. $F_{E,i}$ is the electrostatic force applied on a GNS–CNT hybrid. (b) Schematic illustration of the possible causes for the enhanced adhesion of GNS–CNT hybrids to substrates after the three-step processing. SEM images of the iron catalyst clusters prepared on Fe–Si wafers (c) before and (d) after the 1050 °C and 5 h annealing.

1050 °C for 5 h. Considering the high density and the large area of this sample, this J_{max} is impressive. Furthermore, it can be found that the J_{max} increases monotonously with the annealing temperature and time, indicating that the temperature processing on our samples can greatly ameliorate the adhesion of CNTs to substrates, which will be discussed in the following section. The F–N plots (inset of Figure 7a) exhibit linear relationships at the low-E regions for all types of GNS–CNT hybrids, suggesting that the emission electrons are actually extracted from our emitters by the applied fields.[45] In addition, the FE J–E curves shift to the right with the increase of annealing temperature and time, indicating that the FE performance degrades concomitantly. We ascribe this FE deterioration to the following two aspects. First, the increased testing circles induced deeper aging of emitters. For example, the number of testing circles for the pristine GNS–CNT hybrids is 18, while that for the 1050 °C and 5 h annealed sample is 29. These increased testing circles make the annealed hybrids aged more deeply, and second, the annealing of defects, especially those vacancy-related defects, will decrease the number of active emission sites and thus deteriorate the FE performance.[34,41] Figure 7b shows the FE J–E curves of one of our GNS–CNT hybrids before and after being annealed at 1050 °C for 2 h. It can be seen that the J at 1.75 V/μm drops 3.93 mA/cm^2 and the E at 8 mA/cm^2 increases ~0.04 V/μm after the temperature processing. This FE degradation mainly arises from the annealing of defects, as evidenced by the decreased I_D/I_G ratios (from 1.91 to 1.65) shown in the inset of Figure 7b.

3.5. FE Enhancement Mechanism. The above results show that the J_{max} of CNTs increases from 7.41 to 85.10 mA/cm^2 after the three-step preparation: iron ion prebombardment on Si wafers, compositing with GNSs, and annealing; this FE improvement is ascribed to the enhanced adhesion of CNT emitters to substrates. In the following, a rough calculation will be proposed on the basis of a few assumptions to evaluate this adhesion. Figure 8a schematically shows the electron transfer of GNS–CNT hybrids during FE. The large local applied fields (E_{local}, $E_{local} = \beta E$) at emission sites make electrons aggregate together first and tunnel through barriers and then emit into vacuum. The current breakdown, where we obtain the J_{max}, occurs when part of our emitters are extracted from the array. Assuming that the electric quantity of the aggregated electrons for one GNS–CNT hybrid is q_i, the total electric quantity for the extracted GNS–CNT hybrids is

$$q_{total} = \sum_{i=1}^{N} q_i \quad (1)$$

where N is the total number of the extracted GNS–CNT hybrids. The electrostatic force ($F_{E,i}$) for the q_i hybrid is $F_{E,i} = q_i E_{local,max}$, where $E_{local,max}$ ($E_{local,max} = \beta_i E_{max}$, β_i is the field enhancement factor of this GNS–CNT hybrid) is the local electric field at the tip of this GNS–CNT hybrid when the current breakdown occurs. Here, we ideally assume that every GNS–CNT hybrid has the same β_i equal to the β of the GNS–CNT array; i.e., all GNS–CNT hybrids are perfectly the same. Thus, the total electrostatic force ($F_{E,total}$) for the extracted GNS–CNT hybrids can be expressed as

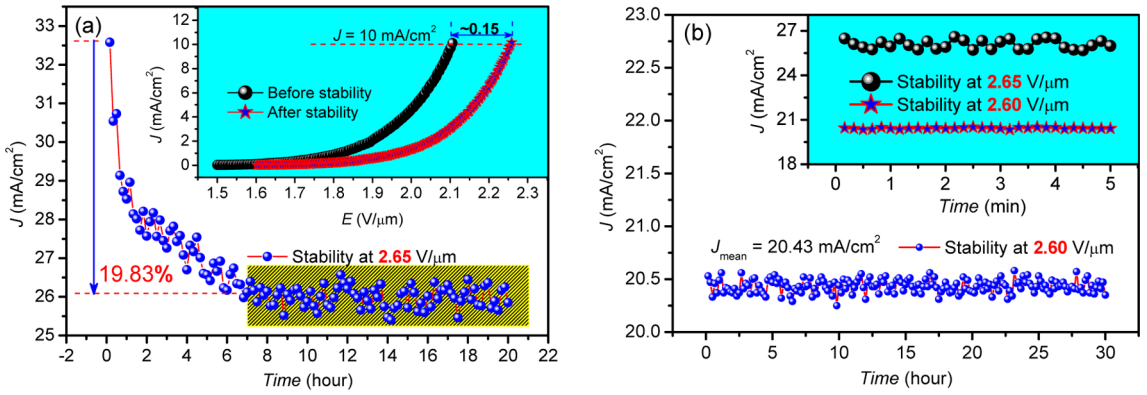

Figure 9. (a) 20 h FE stability at 2.65 V/μm for GNS−CNT hybrids after being annealed at 1050 °C for 5 h. The current density decreases sharply by 19.83% in the first 7 h, while it is relatively stable in the last 13 h (shaded part). The inset is the FE J−E curves of this sample before and after the stability test, the E increases by 0.15 V/μm at 10 mA/cm^2. (b) 30 h FE stability at 2.60 V/μm for the same sample. This stability test was taken right after the first one. The J_{mean} is the mean emission current density. The inset is the 5 min FE stability of this GNS−CNT sample at 2.65 and 2.60 V/μm showing the current fluctuations.

$$F_{E,\text{total}} = \sum_{i=1}^{N} F_{E,i} = \sum_{i=1}^{N} q_i E_{\text{local,max}} = \beta E_{\text{max}} \sum_{i=1}^{N} q_i \quad (2)$$

Assuming the area of the extracted GNS−CNT hybrids is S, the J_{max} for these hybrids is $J_{max} = q_{total}/S$. It is reasonable to assume that this J_{max} is equal to the J_{max} of the GNS−CNT array since the extracted GNS−CNT hybrids are just a part of the array. The $F_{E,total}$ can thus be expressed as follows:

$$F_{E,\text{total}} = \beta E_{\text{max}} S J_{\text{max}} \quad (3)$$

We define a new parameter f_E to characterize the adhesion of CNTs to substrates because the S in eq 3 is hard to determine. The f_E represents the force per unit area applied on the hybrids and is firmly related to the adhesion of hybrids to substrates. It is expressed as

$$f_E = \frac{F_{E,\text{total}}}{S} = \beta E_{\text{max}} J_{\text{max}} \quad (4)$$

According to eq 4, the f_E ratio of CNTs to substrates with and without the three-step processing can be determined: $f_{E,with}/f_{E,without} = 7.37$. We consider that there are two possible causes for this reinforced adhesion, as schematically illustrated in Figure 8b. First, in comparison with the smooth surface of the pristine Si wafers, the defected rough surface of the iron ion bombarded Si wafers makes CNTs easy to grip. Second, part of the bombarded iron will be precipitated from the Fe−Si layer during the high-temperature processing, and these iron residuals tend to gather together in high temperatures to reduce their surface energy, as shown in Figure 8c,d. It can be seen that the catalyst clusters prepared on Fe−Si wafers after being annealed at 1050 °C for 5 h have sizes larger than those of the unannealed ones. We conisder that this gathering of iron residuals can wrap the CNT foot and thus reinforce the adheison of CNTs to substrates, as schematically shown in Figure 8b. The iron residuals here play a role similar to the Ni wetting layer reported previously.[24,25] It should be emphasized that the above evaluation is proposed on the basis of a series of assumptions. The exact quantitative relations among these parameters need to be further understood. However, it is straightforward and reasonable to use this evaluation to analyze the adhesion of CNTs to substrates, especially to compare the adhesions among different types of samples.

3.6. Longtime Stable FE from GNS−CNT Hybrids.

Longtime stable FE is of great importance for emitters in applications. 20 h FE stability for the three-step (iron ion prebombardment, compositing, and annealing at 1050 °C for 5 h) prepared GNS−CNT hybrids (sample area: 4.68 × 10^{-2} cm^2) was tested, as shown in Figure 9a. The constant E was 2.65 V/μm. It can be seen that the J drops sharply by 19.83% in the first 7 h. This is mainly ascribed to the Joule heating induced burning out of active emission sites because of the high emission current.[14,15] The stability test is also an aging process for our emitters. Many active emission sites, such as sp^3-hybridized defects, are removed due to Joule heating, thereby leading to the deterioration of the FE J−E performance of our emitters, as seen from the increased E_{th} of ~0.15 V/μm after the stability test (inset of Figure 9a). On the other hand, the decrease of defects can improve their FE stability. It is really hard to observe the structural change of our emitters before and after the 20 h FE stability test without an *in situ* study in a TEM. We have tried to obtain the structural change of our emitters by using Raman spectroscopy, but the change of Raman spectra before and after the 20 h FE stability test is really negligible, as shown in Figure S2 of the Supporting Information. We consider that the structural change for the GNS−CNT hybrids induced by the aging process is too slight to be determined by the Raman spectroscopy. After the first 7 h aging, the FE current is relatively stable in the following 13 h. It is easy to think that the Joule heating induced burning out of emission sites will be greatly weakened if the FE is further performed at a lower E. In this regard, FE stability at 2.60 V/μm was performed on the same sample for 30 h right after the first stability test, as shown in Figure 9b. It can be seen that the FE current is quite stable at a mean J of 20.43 mA/cm^2. This FE stability from our GNS−CNT hybrids is even better than graphenes,[6] whose two-dimensional structure is believed to be beneficial for stable FE. Furthermore, the current fluctuation for the GNS−CNT hybrids tested at 2.60 V/μm is far smaller than that tested at 2.65 V/μm, as shown in the inset of Figure 9b, mainly because the longtime FE stability test at 2.65 V/μm makes our emitters perfectly aged. Our results suggest that aging at a relatively higher E first and then working at a lower E is an effective approach to improving the FE stability of emitters.

4. CONCLUSIONS

We have demonstrated the preparation of GNS−CNT hybrids by following a process of iron ion prebombardment on Si wafers, self-assembled growth of GNSs on CNTs, and postannealing. CNTs grown on Fe−Si wafers are found to have larger J_{max} than those grown on Si wafers, and the composition of GNSs with CNTs can lower the E_{on} and E_{th} of the CNT emitters. Additionally, the annealing of GNS−CNT hybrids can further increase their J_{max}. An optimal J_{max} up to 85.10 mA/cm^2 is obtained from a 4.65 × 10^{-2} cm^2 GNS−CNT sample, which is far larger than 7.41 mA/cm^2 for the pristine CNTs. This great increase of J_{max} is ascribed to the reinforced adhesion of emitters to substrates. This adhesion for the three-step prepared GNS−CNT hybrids is calculated to be 7.37 times larger than that of the pristine ones. Both the rough surface created by the ion bombardment and the wrapping of CNT foot by catalyst residuals lead to the enhanced adhesion. Furthermore, after being perfectly aged at 2.65 V/μm, the three-step prepared GNS−CNT hybrids exhibit excellent FE stability at 2.60 V/μm with a large J_{mean} of 20.43 mA/cm^2. The large area, the longtime stable FE at high currents, and the relatively low operating fields make our three-step prepared GNS−CNT hybrids good candidates for a wide range of applications such as displays, X-ray tubes, lamps, and so on.

■ ASSOCIATED CONTENT

Ⓢ Supporting Information

The amplified side-view SEM images for CNTs grown on Si and Fe−Si wafers and the Raman spectra for GNS−CNT hybrids before and after the 20 h FE stability test. This material is available free of charge via the Internet at http://pubs.acs.org.

■ AUTHOR INFORMATION

Corresponding Authors

*Phone: +86-22-23766519. E-mail: jhdeng1983@163.com.
*Phone: +86-10-62205403. E-mail: gacheng@bnu.edu.cn.

Notes

The authors declare no competing financial interest.

■ ACKNOWLEDGMENTS

This work was supported by the National Natural Science Foundation of China for Youth Science Funds (51302187), the Key Project of Tianjin Natural Science Foundation (Nos. 14JCZDJC32100 and 13JCZDJC33900), the National Basic Research Program of China (2010CB832905), and partly by the National Natural Science Foundation of China (Nos. 51272176 and 51302188). J.H.-D. also thanks the financial support from the Tianjin Key Laboratory of Structure and Performance for Functional Molecule and the“131” Innovative Talents cultivation of Tianjin.

■ REFERENCES

(1) Iijima, S. Helical Microtubules of Graphitic Carbon. *Nature* **1991**, *354*, 56−58.
(2) Novoselov, K. S.; Geim, A. K.; Morozov, S. V.; Jiang, D.; Zhang, Y.; Dubonos, S. V.; Grigorieva, I. V.; Firsov, A. A. Electric Field Effect in Atomically Thin Carbon Films. *Science* **2004**, *306*, 666−669.
(3) de Heer, W. A.; Châtelain, A.; Ugarte, D. A Carbon Nanotube Field-Emission Electron Source. *Science* **1995**, *270*, 1179−1180.
(4) Baughman, R. H.; Zakhidov, A. A.; de Heer, W. A. Carbon Nanotube—The Route Toward Applications. *Science* **2002**, *297*, 787−792.
(5) Deng, J. H.; Hou, X. G.; Cheng, L.; Wang, F. J.; Yu, B.; Li, G. Z.; Li, D. J.; Cheng, G. A.; Wu, S. L. Irradiation Damage Determined Field Emission of Ion Irradiated Carbon Nanotubes. *ACS Appl. Mater. Interfaces* **2014**, *6*, 5137−5143.
(6) Wu, Z. S.; Pei, S. F.; Ren, W. C.; Tang, D. M.; Gao, L. B.; Liu, B. L.; Li, F.; Liu, C.; Cheng, H. M. Field Emission of Single-Layer Graphene Films Prepared by Electrophoretic Deposition. *Adv. Mater.* **2009**, *21*, 1756−1760.
(7) Liu, J. L.; Zeng, B. Q.; Wu, Z.; Sun, H. Enhanced Field Electron Emission of Graphene Sheets by CsI Coating after Electrophoretic Deposition. *ACS Appl. Mater. Interfaces* **2012**, *4*, 1219−1224.
(8) Liu, P.; Wei, Y.; Liu, K.; Liu, L.; Jiang, K. L.; Fan, S. S. New-Type Planar Field Emission Display with Superaligned Carbon Nanotube Yarn Emitter. *Nano Lett.* **2012**, *12*, 2391−2396.
(9) Jo, G.; Choe, M.; Lee, S.; Park, W.; Kahng, Y. H.; Lee, T. The Application of Graphene as Electrodes in Electrical and Optical Devices. *Nanotechnology* **2012**, *12*, 112001.
(10) Qi, H.; Hegmann, T. Impact of Nanoscale Particles and Carbon Nanotubes on Current and Future Generations of Liquid Crystal Displays. *J. Mater. Chem.* **2008**, *18*, 3288−3294.
(11) Wang, S.; Calderon, X.; Peng, R.; Schreiber, E. C.; Zhou, O.; Chang, S. A Carbon Nanotube Field Emission Multipixel X-Ray Array Source for Microradiotherapy Application. *Appl. Phys. Lett.* **2011**, *98*, 213701.
(12) Wei, Y.; Xiao, L.; Zhu, F.; Liu, L.; Tang, J.; Liu, P.; Fan, S. S. Cold Linear Cathodes with Carbon Nanotube Emitters and Their Application in Luminescent Tubes. *Nanotechnology* **2007**, *18*, 325702.
(13) Kyung, S. J.; Park, J. B.; Park, B. J.; Lee, J. H.; Yeom, G. Y. Improvement of Electron Field Emission from Carbon Nanotubes by Ar Neutral Beam Treatment. *Carbon* **2008**, *46*, 1316−1321.
(14) Dean, K. A.; Burgin, T. P.; Chalamala, B. R. Evaporation of Carbon Nanotubes during Electron Field Emission. *Appl. Phys. Lett.* **2001**, *79*, 1873−1875.
(15) Wang, M. S.; Peng, L. M.; Wang, J. Y.; Chen, Q. Electron Field Emission Characteristics and Field Evaporation of a Single Carbon Nanotube. *J. Phys. Chem. B* **2005**, *109*, 110−113.
(16) Liu, H. B.; Cui, S.; Guo, Y. B.; Li, Y. L.; Huang, C. S.; Zuo, Z. C.; Yin, X. D.; Song, Y. L.; Zhu, D. B. Fabrication of Large-Area Hybrid Nanowires Arrays as Novel Field Emitters. *J. Mater. Chem.* **2009**, *19*, 1031−1036.
(17) Liu, H. B.; Xu, J. L.; Li, Y. J.; Li, Y. L. Aggregate Nanostructures of Organic Molecular Materials. *Acc. Chem. Res.* **2010**, *43*, 1496−1508.
(18) Zheng, H. Y.; Li, Y. J.; Liu, H. B.; Yin, X. D.; Li, Y. L. Construction of Heterostructure Materials toward Functionality. *Chem. Soc. Rev.* **2011**, *40*, 4506−4524.
(19) Guo, Y. B.; Liu, H. B.; Li, Y. J.; Li, G. X.; Zhao, Y. J.; Song, Y. L.; Li, Y. L. Controlled Core−Shell Structure for Efficiently Enhancing Field-Emission Properties of Organic−Inorganic Hybrid Nanorods. *J. Phys. Chem. C* **2009**, *113*, 12669−12673.
(20) Zanin, H.; Saito, E.; Ceragioli, H. J.; Baranauskas, V.; Corat, E. J. Reduced Graphene Oxide and Vertically Aligned Carbon Nanotubes Superhydrophilic Films for Supercapacitors Devices. *Mater. Res. Bull.* **2014**, *49*, 487−493.
(21) Liu, J. L.; Zeng, B. Q.; Wang, X. R.; Wang, W. Z.; Shi, H. L. One-Step Growth of Vertical Graphene Sheets on Carbon Nanotubes and Their Field Emission Properties. *Appl. Phys. Lett.* **2013**, *103*, 053105.
(22) Deng, J. H.; Zheng, R. T.; Zhao, Y.; Cheng, G. A. Vapor-Solid Growth of Few-Layer Graphene Using Radio Frequency Sputtering Deposition and Its Application on Field Emission. *ACS Nano* **2012**, *6*, 3727−3733.
(23) Thong, J. T. L.; Oon, C. H.; Eng, W. K.; Zhang, W. D.; Gan, L. M. High-Current Field Emission from a Vertically Aligned Carbon Nanotube Field Emitter Array. *Appl. Phys. Lett.* **2001**, *79*, 2811−2813.
(24) Lee, H.; Goak, J.; Choi, J.; Kong, B.; Lee, C. H.; Kim, K. B.; Park, J. Y.; Seo, Y.; Choi, Y. C.; Song, Y. H.; Lee, N. High-Current Field Emission of Point-Type Carbon Nanotube Emitters on Ni-Coated Metal Wires. *Carbon* **2012**, *50*, 2126−2133.

(25) Deng, M.; Ding, G.; Wang, Y.; Wu, H.; Yao, Y.; Zhu, L. Fabrication of Ni-Matrix Carbon Nanotube Field Emitters Using Composites Electroplating and Micromachining. *Carbon* **2009**, *47*, 3466−3471.
(26) Fan, S. S.; Chapline, M. G.; Franklin, N. R.; Tombler, T. W.; Cassell, A. M.; Dai, H. J. Self-Oriented Regular Arrays of Carbon Nanotubes and Their Field Emission Properties. *Science* **1999**, *283*, 512−514.
(27) Zhu, W.; Bower, C.; Zhou, O.; Kochanski, G.; Jin, S. Large Current Density from Carbon Nanotube Field Emitters. *Appl. Phys. Lett.* **1999**, *75*, 873−875.
(28) Lee, J.; Jung, Y.; Song, J.; Kim, J. S.; Lee, G. W.; Jeong, H. J.; Jeong, Y. High-Performance Field Emission from a Carbon Nanotube Carpet. *Carbon* **2012**, *50*, 3889−3896.
(29) Sohn, J. I.; Lee, S.; Song, Y. H.; Choi, S. Y.; Cho, K. I.; Nam, K. S. Patterned Selective Growth of Carbon Nanotubes and Large Field Emission from Vertically Well-Aligned Carbon Nanotube Field Emitter Arrays. *Appl. Phys. Lett.* **2001**, *78*, 901−903.
(30) Darbari, S.; Abdi, Y.; Mohajerzadeh, S.; Soleimani, E. A. High Electron Emission from Branched Tree-Like Carbon Nanotubes Suitable for Field Emission Applications. *Carbon* **2010**, *48*, 2493−2500.
(31) Kakade, B. A.; Pillai, V. K.; Late, D. J.; Chavan, P. G.; Sheini, F. J.; More, M. A.; Joag, D. S. High Current Density, Low Threshold Field Emission from Functionalized Carbon Nanotube Bucky Paper. *Appl. Phys. Lett.* **2010**, *97*, 073102.
(32) Okano, K.; Yamada, T.; Ishihara, H.; Koizumi, S.; Itoh, J. Electron Emission from Nitrogen-Doped Pyramidal-Shape Diamond and Its Battery Operation. *Appl. Phys. Lett.* **1997**, *70*, 2201−2203.
(33) Zhirnov, V. V.; Lizzul-Rinne, C.; Wojak, G. J.; Sanwald, R. C.; Hren, J. J. "Standardization" of Field Emission Measurements. *J. Vac. Sci. Technol., B* **2001**, *19*, 87−93.
(34) Kim, G.; Jeong, B. W.; Ihm, J. Deep Levels in the Band Gap of the Carbon Nanotube with Vacancy-Related Defects. *Appl. Phys. Lett.* **2006**, *88*, 193107.
(35) Maiti, A.; Andzelm, J.; Tanpipat, N.; von Allmen, P. Effect of Adsorbates on Field Emission from Carbon Nanotubes. *Phys. Rev. Lett.* **2001**, *87*, 155502.
(36) Deng, J. H.; Yang, Y. M.; Zheng, R. T.; Cheng, G. A. Temperature Dependent Field Emission Performances of Carbon Nanotube Arrays: Speculation on Oxygen Desorption and Defect Annealing. *Appl. Surf. Sci.* **2012**, *258*, 7094−7098.
(37) Suh, J. S.; Jeong, K. S.; Lee, J. S.; Han, I. Study of the Field-Screening Effect of Highly Ordered Carbon Nanotube Arrays. *Appl. Phys. Lett.* **2002**, *80*, 2392−2394.
(38) Tuinstra, F.; Koenig, J. L. Raman Spectrum of Graphite. *J. Chem. Phys.* **1970**, *53*, 1126−1130.
(39) Ferrari, A. C.; Meyer, J. C.; Scardaci, V.; Casiraghi, C.; Lazzeri, M.; Mauri, F.; Piscanec, S.; Jiang, D.; Novoselov, K. S.; Roth, S.; Geim, A. K. Raman Spectrum of Graphene and Graphene Layers. *Phys. Rev. Lett.* **2006**, *97*, 187401.
(40) Nemanich, R. J.; Solin, S. A. First- and Second-Order Raman Scattering from Finite-Size Crystals of Graphite. *Phys. Rev. B* **1979**, *20*, 392−401.
(41) Wei, G. Emission Property of Carbon Nanotube with Defects. *Appl. Phys. Lett.* **2006**, *89*, 143111.
(42) Bertoncello, R.; Casagrande, A.; Casarin, M.; Glisenti, A.; Lanzoni, E.; Mirenghi, L.; Tondello, E. Tin, Tic and Ti (C, N) Film Characterization and Its Relationship to Tribological Behaviour. *Surf. Interface Anal.* **1992**, *18*, 525−531.
(43) Sundberg, P.; Larsson, R.; Folkesson, B. On the Core Electron Binding Energy of Carbon and the Effective Charge of the Carbon Atom. *J. Electron Spectrosc. Relat. Phenom.* **1988**, *46*, 19−29.
(44) Rats, D.; Vandenbulcke, L.; Herbin, R.; Benoit, R.; Erre, R.; Serin, V.; Sevely, J. Characterization of Diamond Films Deposited on Titanium and It's Alloys. *Thin Solid Films* **1995**, *270*, 177−183.
(45) Fowler, R. H.; Nordheim, L. Electron Emission in Intense Electric Fields. *Proc. R. Soc. London, Ser. A* **1928**, *119*, 173−181.
(46) Huang, J. Y.; Kempa, K.; Jo, S. H.; Chen, S.; Ren, Z. F. Giant Field Enhancement at Carbon Nanotube Tips Induced by Multistage Effect. *Appl. Phys. Lett.* **2005**, *87*, 053110.
(47) Zanin, H.; May, P. W.; Hamanaka, M. H. M. O.; Corat, E. J. Field Emission from Hybrid Diamond-Like Carbon and Carbon Nanotube Composite Structures. *ACS Appl. Mater. Interfaces* **2013**, *5*, 12238−12243.